Rapid and quantitative imaging of excitation polarized fluorescence reveals ordered septin dynamics in live yeast

Bradley S. DeMay, Naoki Noda, Amy S. Gladfelter and Rudolf Oldenbourg

Supporting Material

Materials and Methods

Experimental procedures

Yeast strain generation

Generation of constrained septin-GFP fusions was based upon work by Vrabioiu and Mitchison (1,2). 3 amino acids of the N-terminal alpha-helix of GFP and 4 amino acids of the C-terminal region of the septin were deleted to generate what is predicted to be an extended, continuous alpha-helix linking the septin to GFP.

To create strain AGY015 (pAgCDC12-conGFP3) GFP-GEN3 was amplified from plasmid AGB005 (GFP-GEN3) using oligos AGO197 and AGO608. This amplification trimmed 3 amino acids from the N-terminus of GFP while the resulting N-terminus of the PCR product contained homology to the C-terminus of CDC12 so as to truncate the final 4 amino acids (plus the stop codon). This product was co-transformed into yeast with AGB123 (pAgCDC12), yielding AGB228 (pAgCdc12-conGFP3). A verification digest was performed using restriction enzymes NdeI and XmaI (New England BioLabs, Beverly, MA) and the plasmid was sequenced (Dartmouth College Core Facility, Hanover, NH). Following verification of plasmid AGB228, this plasmid was transformed into WT *S. cerevisiae*, creating strain AGY015. A similar procedure using AGO197 and Ago606 was performed to generate pAgCDC12-conGFP4 (AGB229) to make the strain AGY016, with a single amino acid shorter length of the predicted alpha helix bridging GFP and the septin polypeptide. DNA procedures were carried out as described in Sambrook (3). Please refer to **Tables S1-S3** for strain, plasmid, and oligo details. The Cdc12-conGFP septins incorporated into the neck of yeast cells without perturbing cell growth or the appearance of the septin structures indicating that the constrained constructs are likely an accurate report of the organization of the septin cortex.

Table S1. *S. cerevisiae* strains used in this study

Strain	Relevant Genotype	Source
DHD5	*MATa/MATα ura3-52/ura3-52 leu2-3,112/leu2-3,112 his3-11,15/his3-11,15*	(4)
AGY015	DHD5+pAGB228 [pAg*CDC12-conGFP3-GEN3*]	this study
AGY016	DHD5+ pAGB229 [pAg*Cdc12-conGFP4-GEN3*]	this study

Bracketed genotypes denote expression from a plasmid.

Table S2. Plasmids used in this study

Plasmid #	Name	Vector	Relevant Insert	Source
AGB005	pAGT141	pUC19	*GFP-GEN3*	
AGB123	pAg*CDC12*	pRS416	Ag*CDC12*	(5)
AGB228	pAg*CDC12-conGFP3*	pRS416	*conGFP3-GEN3* (3D3)	this study
AGB229	p*AgCDC12-conGFP4*	PRS416	*conGFP4-GEN3* (4D3)	this study

Table S3. Oligonucleotide primers used in this study

Primer #	Name	Sequence 5'-3'
AGO197	5'Cdc1225DSF2a	GTAGTATCGCTGTATATCTTCAACATTGCGATCTGCTGTAAACCACTGCA GGCATGCAAGCTT
AGO608	Cdc123D3GFP-F	CAGGCCAAGGTTAAGAAGCTGGAGGAGCAGGTCAGAGCATTGCAACTAG AAGAACTTTTCACTGGAGTTG
AGO609	Cdc12 4D3 F	CAGGCCAAGGTTAAGAAGCTGGAGGAGCAGGTCAGAGCATTGCAAGA AGAACTTTTCACTGGAGTTG

Specimen culture and preparation.
For polarized fluorescence imaging, *S. cerevisiae* was grown overnight in Yeast Peptone Dextrose (YPD) media and 200μg/ml G418, collected by gravity, and resuspended in 25% YPD, 75% 2x low fluorescence minimal media (LFMM). Cells were transferred to a glass slide, covered with a coverslip (no. 1.5), sealed with Valap, and imaged.

GFP crystal preparation

Purified GFP extracted from the jellyfish *Aequorea* was generously provided by Osamu Shimomura and prepared for observation similar to the description given by Inoué et al. (6). Briefly, 0.5 ml highly purified GFP in sodium phosphate buffer (pH 7.0) was dialyzed in a bag against 20 ml of deionized water contained in a test tube. Every hour, the bag was removed, gently mixed and returned for further dialysis. After 7.5 hours, the water was exchanged with fresh, deionized water and dialysis continued at 4°C. The deionized water was exchanged two more times, with recognizable precipitation after a total of 28 hours of dialysis. To further increase the yield of precipitated crystals, the water was exchanged again and dialysis continued uninterrupted for 38 hours. After one additional water exchange and dialysis for 7.5 hours, the GFP crystal suspension was filled into a glass tube, capped and stored at 4°C.

For observation in the microscope, some precipitate was retrieved from the freshly made stock suspension and placed on a quartz cover-slip. The cover-slip was part of a well slide assembled from a stainless steel plate (25mm x 50mm and 0.7mm thick) with a 15 mm diameter central hole. The well was formed by covering one side of the hole with the quartz cover-slip and sealing it to the metal with Valap. After adding the precipitate and some additional water to the interior of the well, a second quartz cover-slip was placed on top of the hole, capping the well and sealing it with Valap. When making the preparation, we carefully placed the precipitate in

the center of the well and suspended the solution between the two quartz cover-slips without the liquid touching the metal. We observed that GFP crystals were unstable and dissolved within a few hours to days when the suspension was sandwiched between standard glass slides and cover-slips, an observation also reported by Inoué et al. (6). However, GFP crystals suspended in deionized water between two quartz cover-slips at 0.7 mm distance, and surrounded by sealed airspace were stable for many months, with a slow degradation of the crystal morphology visible after several months. The stock solution contained well-formed GFP crystals after being stored in a glass tube at 4°C for more than a year.

Microscopy

For analyzing the orientation and magnitude of polarized fluorescence, we used a standard transmission wide-field microscope equipped with a liquid crystal based universal polarizer in the illumination path. We chose a trans-illumination configuration instead of epi-illumination to avoid the need of a dichroic mirror, which would introduce spurious polarization distortions and reduce the efficiency of fluorescence excitation and emission detection. To minimize background light, we used highly discriminating and efficient interference filters for the excitation (482/18 nm) and emission path (525/45 nm, both BrightLine bandpass filters from Semrock, Rochester NY). To further increase efficiency in measuring anisotropy, we used polarized excitation only, detecting the emitted fluorescence without analyzing its polarization (for a detailed discussion see "Comparison of setup with polarized excitation versus a setup using polarized excitation and parallel polarizer in emission path" later in this Supporting Material). The polarization of the excitation light was set to four linear polarization states, switching the azimuth direction in steps of 45° using the LC universal polarizer (LC-PolScope from Cambridge Research and Instrumentation, now part of Caliper, Hopkinton MA). Images of the emitted fluorescence were recorded with a cooled CCD camera (Retiga EXi, QImaging, Surrey BC) synchronized to the LC-polarizer using a desktop computer with open source image acquisition and processing software (ImageJ (7)) enhanced by custom plugins (CamAcqJ) developed in-house. We used a Microphot SA upright microscope stand (Nikon, Melville NY) equipped with oil immersion optics (Plan Apo 60x objective and apochromat condenser, both 1.4 numerical aperture and selected for low polarization distortions). To maximize the luminance in specimen space, the arc of a xenon high-pressure lamp was focused onto an Ellis light scrambler (Technical Video, Port Townsend WA), whose even output can be directly projected into specimen space by the condenser optics. This "critical illumination" setup maximizes the luminance while optimizing the uniform distribution of light across the full aperture of the high NA condenser.

Calibration of the liquid crystal polarizer

The polarization states of the excitation light were calibrated using a linear polarizing sheet with known transmission axis that was sandwiched between a slide and cover glass and placed as specimen on a rotation stage. The transmission axis of the polarizing sheet was rotated to the first desired orientation and an image of the illuminated polarizer was projected onto the camera using microscope optics. Then the retardance of the LC devices A and B (**Fig. 1a**) were systematically varied, thereby changing the polarization of the illuminating light, until a minimum amount of light passed through the polarizing sheet, making its image on the camera darkest (during calibration the emission filter was removed from the optical path). Three times the orientation of the polarizer was changed by 45° and each time the procedure was repeated and the optimized retardance values of LC-A and LC-B were recorded. This calibration

procedure established the retardance values needed to generate linearly polarized excitation light with polarization azimuth values 0°, 45°, 90°, and 135°. LC devices and camera were under computer control to assist in the calibration and enable fast retrieval of stored retardance values to switch quickly between the four linear polarization states.

Correction of systematic errors when measuring polarized fluorescence

Raw intensity values were corrected for systematic errors, including fluorescence bleaching and differential transmission of microscope optical components. A camera offset recorded at zero light intensity was also subtracted from every image. To be able to correct for fluorescence bleaching, we started the series of image acquisitions with the LC-analyzer setting 0°, followed by 135°, 90° and 45° and ended the series with an additional image I_0' at setting 0°. The loss of intensity between the first and the last image, taken at the same polarization setting, was attributed to fluorescence bleaching. The time interval between each exposure was exactly the same and equal to the exposure time (typ. ~0.6 second) plus a small overhead for image readout. By comparing corresponding intensity values in images I_0 and I_0', the bleach exponent was measured using the following relationship:

$$BleachExp = \ln\left(\frac{< I_0 >}{< I_0' >}\right)/4 ,$$

where $< I_0 >$ and $< I_0' >$ denote intensities averaged over a region that is expected to have the same bleach exponent. Subsequently, images for settings 135°, 90°, and 45° were corrected for bleaching by multiplying appropriate regions with:

$$I_{135}^{BleachCorr} = I_{135} \cdot e^{BleachExp},\ I_{90}^{BleachCorr} = I_{90} \cdot e^{2 \cdot BleachExp},\ I_{45}^{BleachCorr} = I_{45} \cdot e^{3 \cdot BleachExp},$$

where the superscript *BleachCorr* indicates the applied bleach correction.

In our experiments we observed bleach exponents that differed between GFP labeled septins suspended in the cytosol and those assembled into complexes such as the hourglass structure. A further complication arose from the condition that the fluorescence of cortical septin was superimposed on the fluorescence of soluble protein in the cytosol. Therefore, we first analyzed the cytosol fluorescence located near a septin assembly and determined the cytosol's fluorescence magnitude and bleach exponent. We subtracted the cytosol fluorescence from the one observed in septin assemblies and then determined the magnitude, bleach exponent, and anisotropy of the excess fluorescence of septin assemblies in the hourglass, ring, and patch.

A further step in identifying instrument bias and applying error correction is based on the fluorescence of randomly oriented fluorophores, like those suspended in the cytosol. The fluorescence of a large number of randomly oriented fluorophores is unpolarized, leading to the expectation that the fluorescence intensity is the same for every analyzer setting. If this expectation is not borne out by the actual observation, the observed unequal intensities between settings 0°, 45°, 90°, and 135° must be caused by instrument bias, for example by partially polarized excitation light. Therefore, one can derive a correction factor based on the a priori knowledge of isotropic fluorescence from a region with random fluorophores, such as the cytosol. We chose to use the intensity with setting 0° as a reference and derived correction factors using bleach corrected intensity values:

$$InstBias_{45} = \frac{< I_0^{BleachCorr} >}{< I_{45}^{BleachCorr} >},\ InstBias_{90} = \frac{< I_0^{BleachCorr} >}{< I_{90}^{BleachCorr} >},\ InstBias_{135} = \frac{< I_0^{BleachCorr} >}{< I_{135}^{BleachCorr} >},$$

where pointed brackets indicate intensities averaged over many pixels that comprise fluorescence from randomly oriented fluorophores. Pixel intensities in regions with anisotropy are then multiplied by the correction factors to minimize instrument bias:

$$I_{45}^{BleachCorr,InstBias} = InstBias_{45} \cdot I_{45}^{BleachCorr},$$
$$I_{90}^{BleachCorr,InstBias} = InstBias_{90} \cdot I_{90}^{BleachCorr},$$
$$I_{135}^{BleachCorr,InstBias} = InstBias_{135} \cdot I_{135}^{BleachCorr}.$$

The intensity values corrected for bleaching and instrument bias were entered into the expressions for *anisotropy*, *ratio* and *azimuth*, given in the main text. Regarding the GFP crystal fluorescence, shown in **Figure 1c**, we observed no measurable bleaching during exposure, and background fluorescence was negligible.

Additional sources of errors that mainly affect the magnitude of the measured anisotropy, but not the measured azimuth of preferred orientation, include the divergence of the excitation and emission beam used in microscope optics. The divergence is expressed by the numerical aperture of the microscope condenser and objective lens, for which we use oil immersion optics with a numerical aperture of up to 1.4. The main effect of high NA optics on measurements of polarized fluorescence is the reduction of the measured anisotropy (8). With increasing numerical aperture and beam divergence, the range of angles subtended by the excitation and imaging beam increases and is superimposed in a single measurement. In other words, the higher the NA the less sensitive the measurement scheme becomes to anisotropy and the lower the value measured for a given anisotropic fluorophore distribution. However, the reduction applies essentially equally to all distributions, regardless of their fluorophore arrangements and orientations, and therefore does not appreciably affect the patterns of anisotropy considered here. Furthermore, the numerical aperture does not affect the orientation of the anisotropy or azimuth angle that is measured for a given distribution. The azimuth mainly depends on the angle between the central ray of the polarized illumination beam that travels parallel to the Z-axis and the orientation distribution of the dipole moments.

While septin assemblies remain unchanged over a time span of several seconds, it is known that septin molecules in the higher order structures can exchange against septins from the surrounding cytosol, particularly at assembly and before cytokinesis (9-11). If an ordered yet dynamic structure is being analyzed, the association/dissociation of proteins results in a potential reduction of the measured anisotropy. If a significant fraction of labeled proteins exchange during the acquisition time, the contribution of light from GFP dipoles not constrained by the architecture of the structure increases. The detection of this extra light would generally result in the addition of an isotropic light component and reduce the measured anisotropy. In a recent study of septin structures in different cell types we bleached the fluorescence of septin-GFP constructs to test the exchange rate between septins in higher order structures against cytosolic septins. We found a measurable but moderate rate of fluoresccence recovery after photo bleaching in the filamentous fungus *A. gossypii*, recovering its fluorescence over a minute or so (9). Hence, during acquisition times of up to 5 sec, septin exchange should only play a minor role in affecting the anisotropy ratio.

Comparison of setup with polarized excitation versus a setup using polarized excitation and parallel polarizer in emission path

We compare the expected relative error of anisotropy measurements using a setup with an excitation polarizer only, called setup A, versus a setup B that uses two parallel polarizers, one in the excitation and one in the emission path. While setup B suffers from some light loss due to the polarizer in the emission path, Inoué (6) has shown that the intensity ratio measured for GFP crystals in a setup of type B can in fact be much larger, almost the square of the ratio measured for the same sample using a setup of type A with a single polarizer only. Therefore it is interesting to ask: Are there circumstances in which the higher polarization ratio provided by setup B would make it preferable to A, despite the extra light loss associated, or is setup A superior under all conceivable circumstances with all possible samples?

For estimating the standard deviation of anisotropy ratios measured with either setup, we assume that shot noise of the recorded fluorescence is the dominant noise source. We further assume that with either setup the exposure to excitatory polarized light is the same, leading to the same amount of photo bleaching or toxicity. As reference we use the polarizer orientation that results in a maximum of acquired photons, an orientation that is the same for both setups and is equal to the *azimuth* angle. However, the same excitatory exposure applied with setup B results in a reduced photon count compared to setup A because of the additional analyzer in the emission path of B. To estimate the reduction in photon count we consider an ensemble of randomly oriented fluorophores that is illuminated with linearly polarized light and make a few additional simplifying assumptions: the transition moments of the fluorophores have dipole characteristics, the molecular excitation and emission dipoles are collinear, and the time constant of rotational diffusion of the fluorphores is much longer than the fluorescent lifetime. With these assumptions, the ratio of intensities measured with setup B using parallel versus perpendicular analyzer is 3 to 1 (12). In other words, under ideal circumstances, the relative intensity measured with setup A featuring no analyzer is 3+1=4, while the relative intensity measured with setup B is 3. Hence, the reduction in intensity measured with setup B is equivalent to multiplying the photon count measured with setup A by a factor ¾ or 0.75. This does not take into account, however, that the non-ideal analyzer also absorbs typically 20% of the photons with polarization parallel to the analyzer, further reducing the photon count. On the other hand, this effect might be canceled by the fact that the ensemble of fluorophores contributing to the measured fluorescence is not really random, but exhibits some anisotropy that increases the relative photon count for setup B. We assume the two effects approximately balance each other out and we use the factor 0.75, which possibly underestimates the reduction when considering fluorophore ensembles that are nearly isotropic representing the most challenging experimental situation.

With these assumptions we calculated the statistical uncertainty in the measured intensity ratios by assuming a Poisson distribution for the number of photons representing the maximum and minimum intensities. Because of the non-linear nature of a Poisson distribution, especially for low photon counts, we estimated the uncertainty by repeatedly calculating ratios R with average photon count N in the maximum of setup A, and a reduced photon count for setup B:

$$\text{setup A: } R_A = \frac{I_{\max}}{I_{\min}} = \frac{[N]}{[N/r]}$$

$$\text{setup B: } R_B = \sqrt{\frac{I_{\max}}{I_{\min}}} = \sqrt{\frac{[0.75\,N]}{[0.75\,N/r^2]}}$$

where r is the nominal ratio for which the uncertainty is determined. The factor 0.75 accounts for the reduced photon count with setup B, as discussed above. Photon counts with square brackets were repeatedly generated assuming a Poisson distribution around an average indicated by the number in the bracket. Each simulated photon count was generated independently. Based on a large number (1000) of simulated counts, ratios R_A, R_B and their mean and standard deviation were calculated. The relative standard deviation (std. dev.)/(mean) was then plotted as a function of N and the ratio r and is shown in **Fig. S1**. It is interesting to note that for $r > 3$, ratios simulated for setup A have a smaller relative standard deviation than those for setup B, while for $r < 3$ it is the other way around. This effect is caused by the large relative std. dev. of the intensity minimum. Since for setup B the intensity ratio is the square of r, the intensity minimum decreases steeply for large r, leading to a dramatic increase in its relative std. dev., which then dominates the error of the measured ratio R_B.

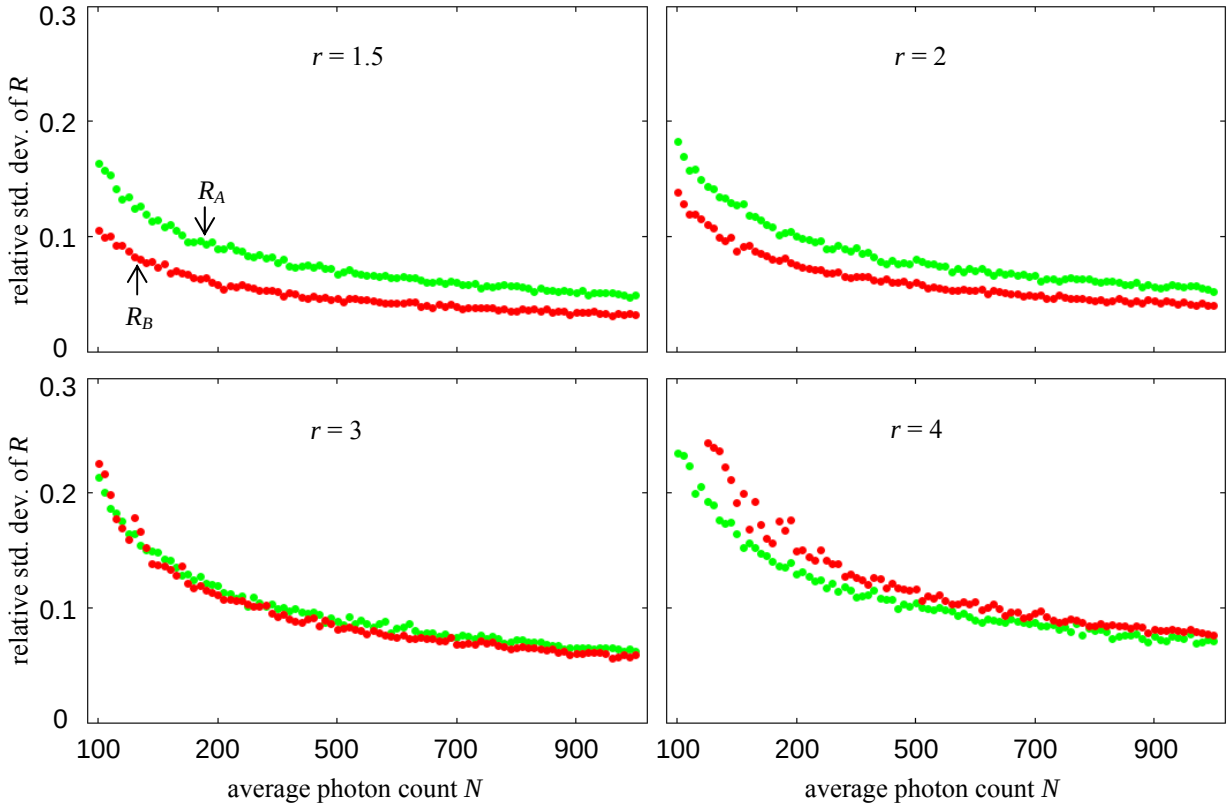

Figure S1. Relative standard deviation of simulated ratio values for setup A (green) and B (red) versus average photon count in intensity maximum, with nominal ratio values r ranging from 1.5 to 4

To explore the effect of background light that is independent of the polarizer/analyzer angle, we added a constant photon count $f\,N$ that is assumed to be a fraction f of I_{max} and used the following modified expressions for R_A and R_B:

$$\text{setup A: } R_A = \frac{I_{\max} - bg}{I_{\min} - bg} = \frac{[N] - f\,N}{[(1-f)N/r + f\,N] - f\,N}$$

$$\text{setup B: } R_B = \sqrt{\frac{I_{\max} - bg}{I_{\min} - bg}} = \sqrt{\frac{[0.75\,N] - f\ 0.75\,N}{[((1-f)0.75\,N)/r^2 + f\,0.75\ N] - f\,0.75\ N}}$$

The calculated relative std. dev. for those expressions are plotted in **Fig. S2**.

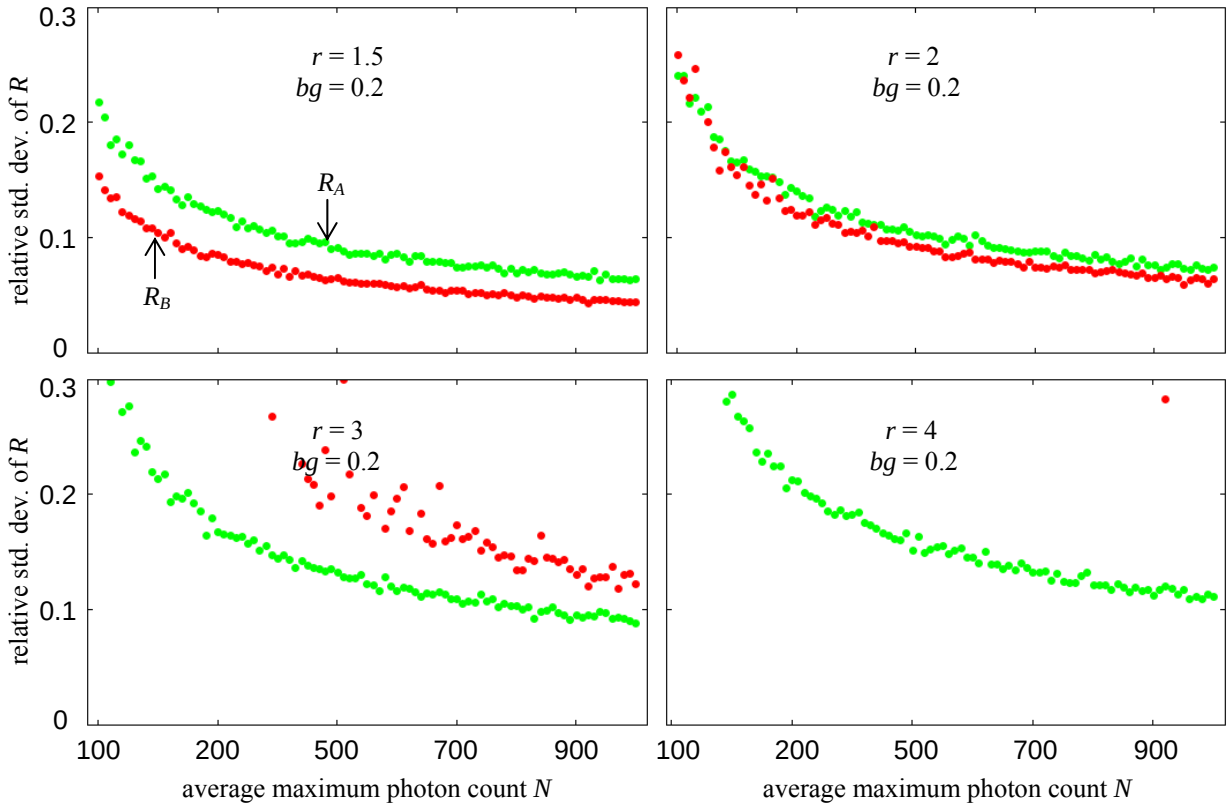

Figure S2. Relative standard deviation of simulated ratio values for setup A (green) and B (red) versus average photon count in intensity maximum, with nominal ratio values r and a constant background fraction of 0.2 of the maximum count N.

The results of the simulation with a background fraction of 0.2 show that the "brake even" point is now $r \approx 2$, with an advantage for setup A when $r > 2$, and an advantage for B when $r < 2$. The relative std. dev. of setup B and $r = 4$ is off the chart, because of the overwhelming uncertainty in I_{min} after subtracting the background contribution. We also note that the advantage for setup B when measuring low ratios becomes more tenuous when only a low number of photons can be counted.

At this point it seems that there are distinct advantages for setup A and B, depending on the expected ratio to be measured and amount of background fluorescence. However, the increased complexity of setup B, in which both polarizers have to be synchronously rotated, and the more complicated analytic expression with a cosine square and fourth power term that has to be fitted, make the advantage gained with setup B questionable. Furthermore, it is not clear to what extent the square relationship between the two intensity ratios holds when making measurements on systems with low anisotropy using high NA optics. These and other questions should be addressed through additional experimental and theoretical investigations.

Theoretical Modeling

Calculating anisotropy values based on GFP dipole orientations

GFP exhibits a linear dipole transition moment (13) and preferentially absorbs and emits polarized light. The polarization dependent absorption of a single dipole was modeled after the radiation pattern of a linear dipole using vector algebra as discussed, for example, in (14). Accordingly, the vectorial extinction coefficient $\vec{\varepsilon}$ is proportional to the vector cross products between the dipole moment $\vec{p}$, and the direction $\vec{x}$ of the incoming radiation:

$$\vec{\varepsilon} = C\,\vec{x} \times \vec{p} \times \vec{x}.$$

The three vector components of $\vec{\varepsilon}$ correspond to the extinction coefficients for the three vector components of the electric field amplitude of a light wave impinging on the dipole and propagating in the direction $\vec{x}$. Since we are only interested in the orientation dependence of $\vec{\varepsilon}$, we set the proportionality constant C and the lengths of vectors $\vec{p}$ and $\vec{x}$ all equal to 1. Furthermore, in the laboratory frame of reference, we set the direction of the incoming light parallel to the Z-axis. The anisotropy of absorption for a given dipole orientation was calculated by first projecting the extinction $\vec{\varepsilon}$ onto 4 polarization directions in the X-Y plane, each rotated by 45° around Z, and squaring the results:

$$\varepsilon_0^2 = \left(\vec{\varepsilon}\cdot\begin{bmatrix}1\\0\\0\end{bmatrix}\right)^2, \varepsilon_{45}^2 = \left(\vec{\varepsilon}\cdot\begin{bmatrix}\sqrt{0.5}\\\sqrt{0.5}\\0\end{bmatrix}\right)^2, \varepsilon_{90}^2 = \left(\vec{\varepsilon}\cdot\begin{bmatrix}0\\1\\0\end{bmatrix}\right)^2, \varepsilon_{135}^2 = \left(\vec{\varepsilon}\cdot\begin{bmatrix}-\sqrt{0.5}\\\sqrt{0.5}\\0\end{bmatrix}\right)^2.$$

The projected and squared extinction coefficients $\varepsilon_0^2, \varepsilon_{45}^2, \varepsilon_{90}^2, \varepsilon_{135}^2$ are proportional to the absorbed excitation light, which in turn is proportional to the total emitted fluorescence intensity. Hence, we inserted $\varepsilon_0^2, \varepsilon_{45}^2, \varepsilon_{90}^2, \varepsilon_{135}^2$ into expression (2) each taking the role of intensities I_0, I_{45}, I_{90}, I_{135}, respectively. Subsequently the anisotropy and azimuth values were calculated using expressions (3) and (4).

In our measurements, the anisotropy within an optically resolved region is the result of superimposing the absorption of many fluorophores located within the resolved region. Since the absorption of separate fluorophores occurs mutually independent or incoherently, the extinction coefficients of individual fluorophores can be added up like intensities. Hence, we modeled the absorption of many superimposing fluorophores as incoherent events and calculated the combined likelihood of absorption by adding the squared extinction coefficients of the individual

fluorophores. As described in the main text, within an optically resolved region of the hourglass or split ring assembly, fluorophores have only four prevailing orientations, which are described by a single pair of angles θ and ϕ. Hence, the anisotropy patterns were calculated using intensities based on four dipole orientations described by two angles θ and ϕ, plus an additional constant intensity representing unpolarized background light. The constant background intensity was chosen to be 2.5% of the maximum intensity contributed by a single dipole. Increasing the background intensity reduces the anisotropy value but does not affect its computed orientation.

Modeling Results

In addition to **Figs. 6** and **7** in the main text, **Figs. S3** to **S5** present further results of our modeling efforts.

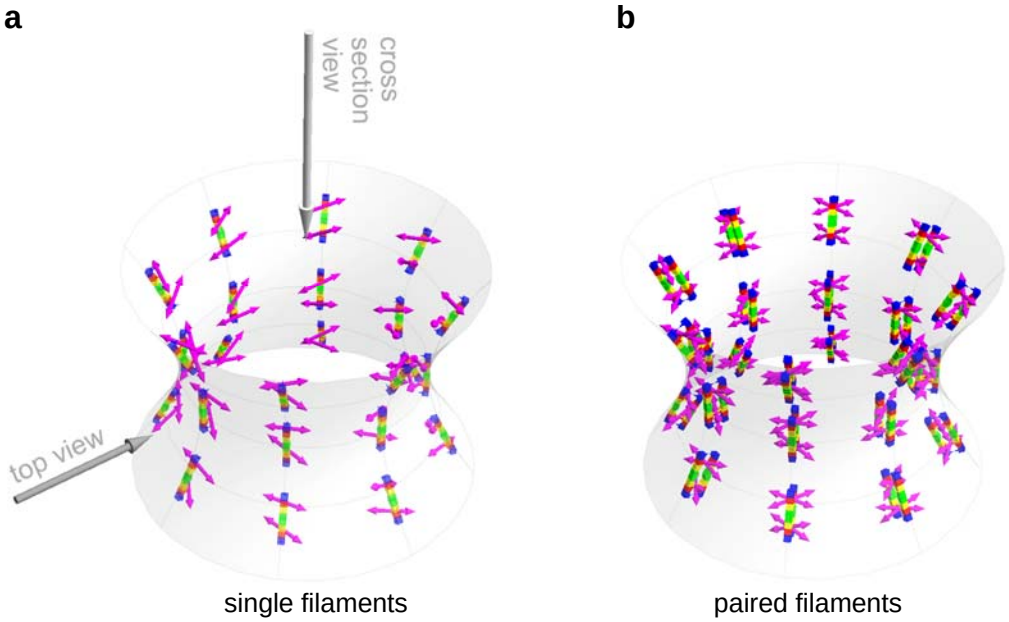

Figure S3. Schematics illustrating hourglass arrangements of single and paired septin filaments with GFP dipoles connected to Cdc12 termini in the yeast bud neck. Filaments are aligned parallel to the surface and to the projection of the hourglass axis. Perspective views of (**a**) single filaments and (**b**) paired filaments.

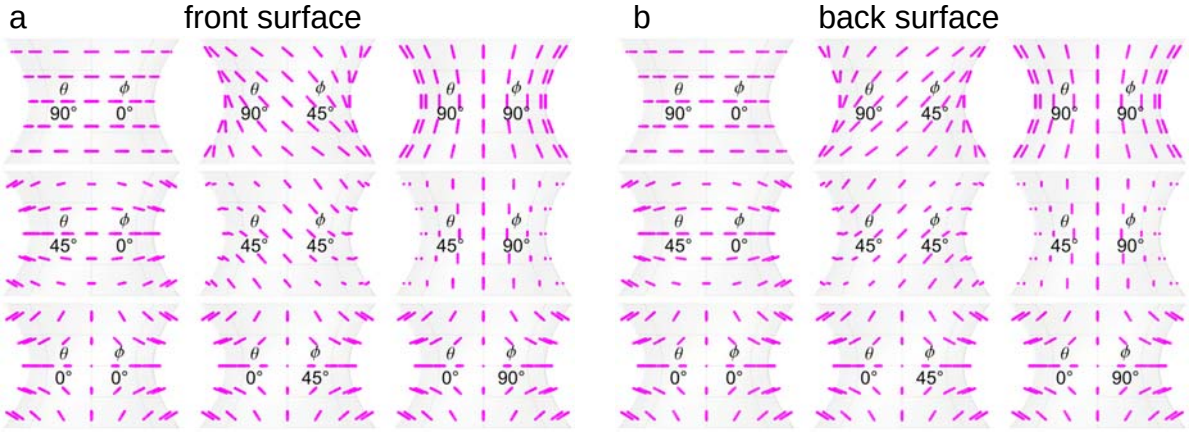

Figure S4 Calculated anisotropy patterns of single septin filaments in hourglass top view as a function of the GFP dipole orientation. The lengths of the magenta lines are proportional to the *anisotropy*, their orientations are parallel to the polarization that exhibits the strongest fluorescence. Orthographic projections of (**a**) the front surface and (**b**) the back surface for θ and ϕ values indicated. Note the flip in diagonal orientation between front and back surface.

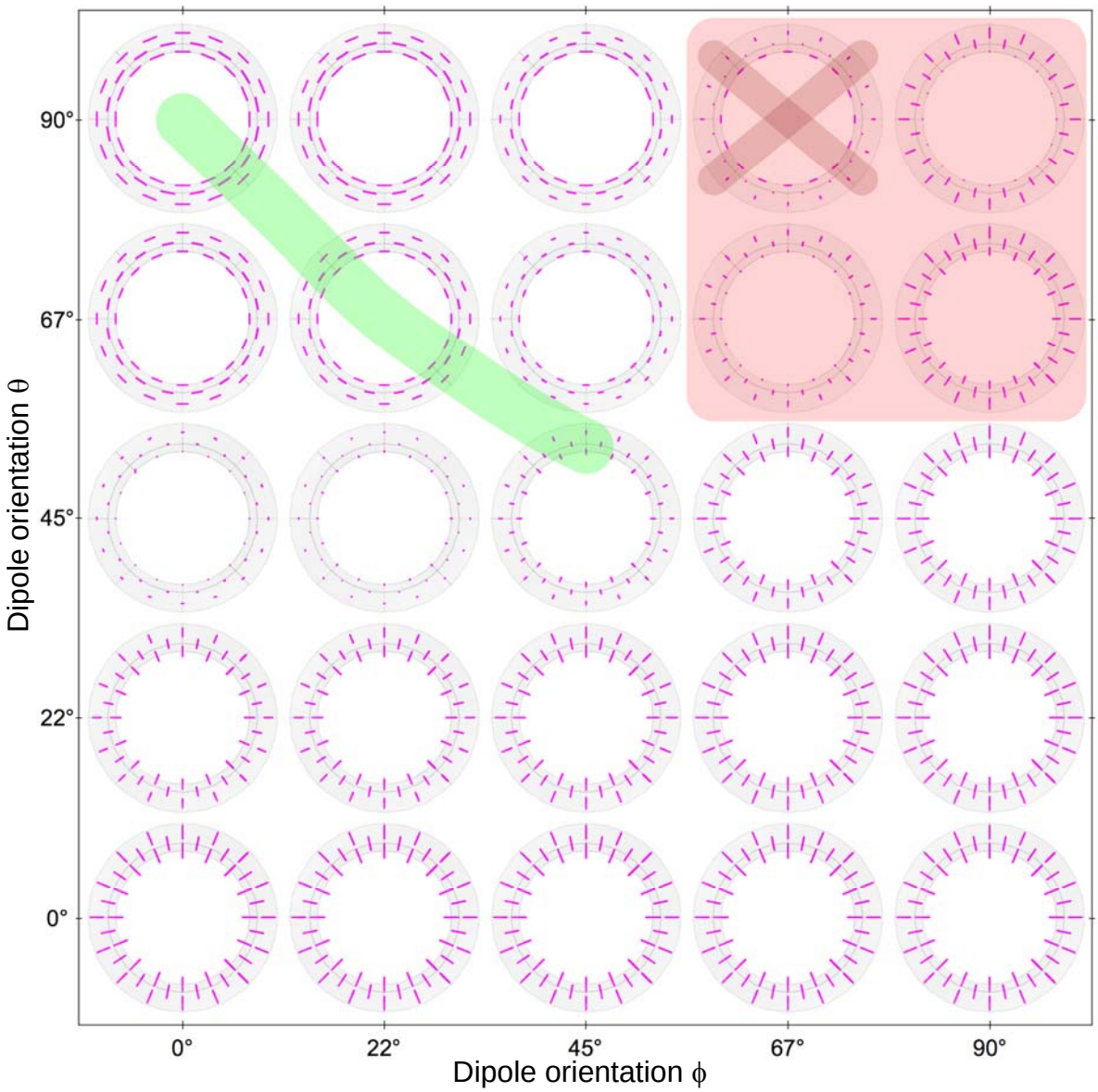

Figure S5 Map of calculated anisotropy patterns in cross section view as a function of the GFP dipole orientation. Paired filaments run nearly parallel to hourglass axis. Hourglass schematics with anisotropies are drawn on a grid of θ and ϕ values. The red rectangle outlines {θ, ϕ} value pairs that generated anisotropy patterns that are compatible with measured patterns of the Cdc12-conGFP3 construct in top view (see also **Fig. 7** in main text). However, when viewed in cross-section, the range of compatible {θ, ϕ} values is reduced compared to the compatible range in top view. In cross section view, the calculated pattern generated using {90°, 67°} is incompatible with the measured pattern. {θ, ϕ} values associated with the green strip are compatible with CDC12-conGFP4 measurements in both, top (**Fig. 7)** and cross-section view.

Movie Captions

Movie S1 The raw fluorescence data (corrected for photobleaching) of the top view of a septin hourglass (incorporating Cdc12-conGFP4) depicted in Figure 3a has been compiled into a

QuickTime movie for viewing the changes in fluorescence across the hourglass depending upon the polarization angle of the excitatory light, which is shown at the bottom left.

Movie S2 The raw fluorescence data (corrected for photobleaching) of the cross-section view of a septin ring (incorporating Cdc12-conGFP4) depicted in Figure 3a has been compiled into an QuickTime movie for viewing the changes in fluorescence across the ring depending upon the polarization angle of the excitatory light, which is shown at the bottom left.

Movies S3-S7 The raw fluorescence data collected from excitation at each polarization angle for each of the sequences of septin ring state depicted in Figure 4 are compiled in 5 QuickTime movies for viewing the differences in emission depending on ring orientation and state. The movies are numbered sequentially such that Movie 3 is the top row of images in Figure 4 and Movie 7 is the bottom row. It should be noted that these images have been bicubically interpolated to better display the shape of the septin ring and have not been corrected for differences in transmission or photobleaching.

References

1. Vrabioiu, A. M. and T. J. Mitchison. 2006. Structural insights into yeast septin organization from polarized fluorescence microscopy. Nature 443:466-469.

2. Vrabioiu, A. M. and T. J. Mitchison. 2007. Symmetry of septin hourglass and ring structures. Journal of Molecular Biology 372:37-49.

3. Sambrook, J. and D. Russell. 2001. Molecular Cloning: A Laboratory Manual. Cold Spring Harbor, NY: Cold Spring Harbor Laboratory Press.

4. Schmitz, H. P., A. Kaufmann, M. Kohli, P. P. Laissue, and P. Philippsen. 2006. From function to shape: a novel role of a formin in morphogenesis of the fungus Ashbya gossypii. Molecular Biology of the Cell 17:130-145.

5. DeMay, B. S., R. A. Meseroll, P. Occhipinti, and A. S. Gladfelter. 2009. Regulation of distinct septin rings in a single cell by Elm1p and Gin4p kinases. Molecular Biology of the Cell 20:2311-2326.

6. Inoue, S., O. Shimomura, M. Goda, M. Shribak, and P. T. Tran. 2002. Fluorescence polarization of green fluorescence protein. Proc Natl Acad Sci U S A 99:4272-4277.

7. Rasband, W. S. 2009. ImageJ. Bethesda MD, USA: U. S. National Institutes of Health.

8. Axelrod, D. 1979. Carbocyanine dye orientation in red cell membrane studied by microscopic fluorescence polarization. Biophys J 26:557-573.

9. DeMay, B. S., X. Bai, L. Howard, P. Occhipinti, R. A. Meseroll, E. T. Spiliotis, R. Oldenbourg, and A. S. Gladfelter. 2011. Septin filaments exhibit a dynamic, paired organization that is conserved from yeast to mammals. J. Cell Biol. 193:1065-1081.

10. Caviston, J. P., M. Longtine, J. R. Pringle, and E. Bi. 2003. The role of Cdc42p GTPase-activating proteins in assembly of the septin ring in yeast. Mol Biol Cell 14:4051-4066.

11. Dobbelaere, J., M. S. Gentry, R. L. Hallberg, and Y. Barral. 2003. Phosphorylation-dependent regulation of septin dynamics during the cell cycle. Dev Cell 4:345-357.

12. Lakowicz, J. R. 2006. Principles of Fluorescence Spectroscopy. New York: Springer.

13. Rosell, F. I. and S. G. Boxer. 2003. Polarized absorption spectra of green fluorescent protein single crystals: transition dipole moment directions. Biochemistry 42:177-183.

14. Jackson, J. D. 1999. Classical Electrodynamics. New York: John Wiley and Sons, Inc.